A Journal of the Gesellschaft Deutscher Chemiker

Angewandte International Edition GDCh Chemie

www.angewandte.org

Accepted Article

Title: Charge Reservoirs in an Expanded Halide Perovskite Analog: Enhancing High-Pressure Conductivity through Redox-Active Molecules

Authors: Roc Matheu, Feng Ke, Aaron Breidenbach, Nathan Wolf, Young Lee, Zhenxian Liu, Linn Leppert, Yu Lin, and Hemamala Karunadasa

To be cited as: *Angew. Chem. Int. Ed.* **2022**, e202202911

Link to VoR: https://doi.org/10.1002/anie.202202911

WILEY-VCH

WILEY-VCH

COMMUNICATION

Charge Reservoirs in an Expanded Halide Perovskite Analog: Enhancing High-Pressure Conductivity through Redox-Active Molecules

Roc Matheu,[a] Feng Ke,[b,c] Aaron Breidenbach,[b,d] Nathan R. Wolf,[a] Young Lee,[b,e] Zhenxian Liu,[f] Linn Leppert,[g] Yu Lin,[b] and Hemamala I. Karunadasa[a,b]

[a] Dr. R. Matheu, Dr. N. R. Wolf, and Prof. H. I. Karunadasa
Department of Chemistry
Stanford University, Stanford, California 94305, United States
Email: rmatheu@stanford.edu, hemamala@stanford.edu
[b] Dr. F. Ke, Mr. A. Breidenbach, Dr. Y. Lin, Prof. Y. Lee, and Prof. H. I. Karunadasa
Stanford Institute for Materials and Energy Sciences, SLAC National Accelerator Laboratory
Menlo Park, CA 94025, United States
[c] Dr. F. Ke
Department of Geological Sciences
Stanford University, Stanford, CA 94305, USA
[d] Mr. A. Breidenbach
Department of Physics
Stanford University, Stanford, CA 94305, USA
[e] Prof. Y. Lee
Department of Applied Physics
Stanford University, Stanford, CA 94305, USA
[f] Prof. Z. Liu
Department of Physics
University of Illinois at Chicago, Chicago, IL 60607, USA
[g] Dr. L. Leppert
MESA+ Institute for Nanotechnology, University of Twente
7500 AE Enschede, The Netherlands

Supporting Information for this article is given via a link at the end of the document.

Abstract: *As halide perovskites and their derivatives are being developed for numerous optoelectronic applications, controlling their electronic doping remains a fundamental challenge. Herein, we describe a novel strategy of using redox-active organic molecules as stoichiometric electron acceptors. The cavities in the new expanded perovskite analogs (dmpz)[Sn_2X_6], (X = Br^- (**1Br**) or I^- (**1I**)) are occupied by $dmpz^{2+}$ (N, N′-dimethylpyrazinium), with the LUMOs lying ca. 1 eV above the valence band maximum (VBM). Compressing the metal-halide framework drives up the VBM in **1I** relative to the dmpz LUMO. The electronic conductivity increases by a factor of 10^5 with pressure, reaching 50(17) S cm^{-1} at 60 GPa, exceeding the high-pressure conductivities of most halide perovskites. This conductivity enhancement is attributed to an increased hole density created by $dmpz^{2+}$ reduction. This work elevates the role of organic cations in 3D metal-halides, from templating the structure to serving as charge reservoirs for tuning the carrier concentration.*

As halide perovskites are developed for a range of optoelectronic applications, including as key components in solar-cells and light-emitting diodes,[1-3] a greater understanding of how to control their transport properties is needed.[4] Such advances will improve the performance of these semiconductors in current applications and open myriad new possibilities.[4-6] In particular, achieving a high concentration of charge carriers (holes or electrons) through controlled electronic doping requires further development.[6] Electronic doping in halide perovskites mainly relies on defect formation (intrinsic doping) and impurity incorporation (extrinsic doping). For example, the high conductivity of the 3D perovskite $(CH_3NH_3)SnI_3$[7] (Figure 1A) occurs through *p*-doping due to the simultaneous formation of Sn^{4+} centers and Sn^{2+} vacancies,[6, 8-9] as also seen in the analogous 2D Sn perovskites.[10] Another strategy involves charge-transfer doping, where carriers are exchanged between the perovskite and an external acceptor/donor, such as a metal-oxide or a molecule.[6] For molecular charge-transfer *p*-doping, the lowest unoccupied molecular orbital (LUMO) of the acceptor molecule must lie close to the valence band maximum (VBM) of the semiconductor, triggering charge transfer and increasing the hole concentration in the semiconductor. This type of doping occurs at the surface of the semiconductor crystallites. To use a charge-transfer dopant throughout a bulk semiconductor, we sought to incorporate redox-active molecules as part of the crystal structure. Herein, we describe (dmpz)[Sn_2X_6] (**1X**, X = Br^- and I^-, Figure 1B); an expanded analog of a halide perovskite containing redox-active cations (*N*, *N*′-dimethylpyrazinium, $dmpz^{2+}$). At ambient pressure, the $dmpz^{2+}$ LUMO lies 0.84 eV above the VBM in **1I**. Upon compression in a diamond-anvil cell (DAC), the VBM approaches the dmpz LUMO, reducing the lowest-energy optical gap, and the conductivity increases by five orders of magnitude, reaching 50(17) S cm^{-1} at 60 GPa, considerably exceeding the values achieved by related perovskites at high pressures (e.g., $(CH_3NH_3)PbI_3$, 6.6 S cm^{-1} at 62 GPa).[11] Altogether, we assess how the redox activity of the organic cations may enhance high-pressure conductivity through internal charge-transfer doping.

We,[12] and others[13-15] recently reported expanded 3D perovskite analogs, where a single metal-halide octahedron in the $A^IB^{II}X_3$ perovskite is replaced by a dimer of edge-sharing octahedra, which propagate through shared corners to afford the $A^IB^{II}X_3 \times 2$

10.1002/anie.202202911

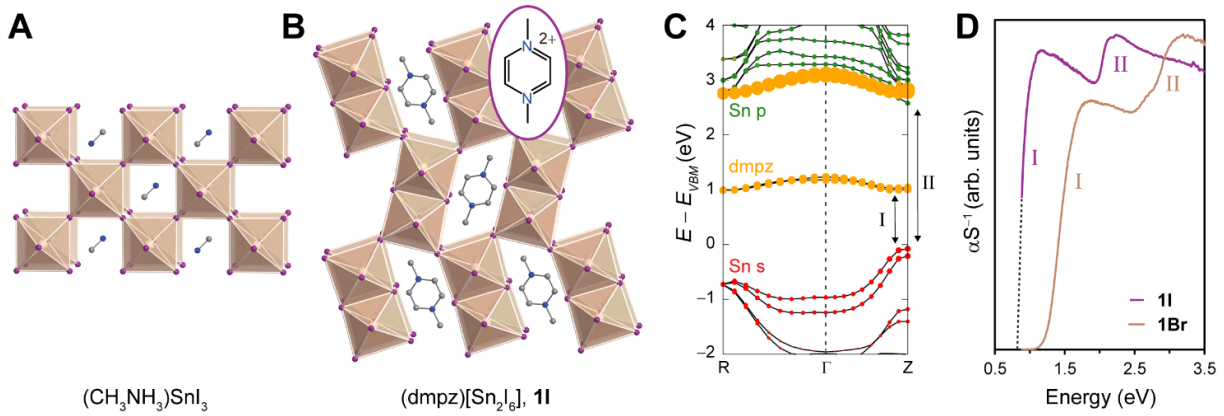

Figure 1. A) Crystal structure of the 3D perovskite $(CH_3NH_3)SnI_3$. B) Crystal structure of an expanded analog of a 3D halide perovskite: (dmpz)[Sn_2I_6] (**1I**) reported here; C) Electronic band structure for **1I**, calculated using density functional theory (DFT). The two possible optical transitions are labeled as Ⅰ and Ⅱ. Contributions from Sn-5s and -5p orbitals and dmpz orbitals are shown in color. Contribution from the halide orbitals is not shown for clarity; D) Diffuse-reflectance spectra for **1I** and (dmpz)[Sn_2Br_6] (**1Br**). The diffuse reflectance data were transformed using the Kubelka–Munk function (α and S are the pseudo-absorption and scattering coefficients, respectively). The low-energy spectrum for **1I** was below the instrument detection limit and was extrapolated (dotted line).

→ $A^{I}_2B^{II}_2X_6$ → $A^{II}B^{II}_2X_6$ structure (Figure 1B). Unlike 3D perovskites, only holding small cations in the framework cavities (e.g., $CH_3NH_3^+$), the expanded analogs accommodate larger aromatic dications with low-lying π* orbitals, including redox-active pyrazinium derivatives such as $dmpz^{2+}$.[12] In prior work, we found that the π* LUMO of $dmpz^{2+}$ composes the flat conduction band in (dmpz)[Pb_2Br_6], whereas states from the inorganic Pb–Br framework form the VBM. We hypothesized that this electronic structure could create mobile holes in the valence band by inducing electron transfer to the organic cations. Thus, we synthesized the Sn^{2+} analogs, which were expected to hole dope easily, in analogy to $(CH_3NH_3)SnI_3$.[8]

Under air-free conditions, powders and crystals of **1X** were obtained by combining $dmpz(BF_4)_2$ and SnX_2 (X = Br^-, I^-) solutions in the respective concentrated hydrohalic acid, except for **1Br** crystals formed in acetonitrile (Supporting Information). The **1X** structures, elucidated by single-crystal X-ray diffraction (SCXRD),[16] consist of isolated $dmpz^{2+}$ cations and a 3D inorganic framework of corner-sharing Sn–X octahedra dimers (Figure 1B and S1), akin to the reported Pb analogs.[12] The phase purity of the powders was confirmed using powder X-ray diffraction (PXRD) (Figures S2 – S3) and CHN elemental analysis (Supporting Information).

We calculated electronic band structures for **1X** using density functional theory (DFT) (Figure 1C and S24) based on the PBE0 functional modified with 35% exact exchange (Supporting Information). The **1X** electronic band structures show that the VBM consists of Sn-s and halide-p orbitals, like in 3D Sn–X perovskites.[17-18] In contrast to the ABX_3 perovskites, the lowest unoccupied band for **1I** consists of empty $dmpz^{2+}$ π* orbitals, lying ~1 eV above the VBM, affording an inorganic-to-organic optical transition (Ⅰ) and an inorganic-to-inorganic transition at higher energies (Ⅱ). Similarly, the **1Br** electronic structure shows two transitions, albeit at higher energies than for **1I** (Figure S24). For **1X**, the higher-energy transition Ⅱ may also involve LUMO+*n* empty orbitals in $dmpz^{2+}$ (Figures 1C and S24).

We measured the diffuse reflectance spectra for **1X** under air-free conditions. As the electronic structures predicted, the spectra revealed two bands (Figure 1D). We estimated the optical gap (transition Ⅰ; E_g) through the Tauc method for direct bandgap semiconductors (Figure S4).[12, 19] Like in 3D perovskites, the iodide derivative exhibits a smaller gap than the bromide owing to the halide orbital contribution to the VBM.[17-18, 20] Further, the two optical transitions for **1X** are ~0.4 – 0.6 eV lower in energy than the corresponding transition energies for (dmpz)[Pb_2X_6],[12] likely due to the greater relativistic stabilization of the Pb 6s orbitals compared to the Sn 5s orbitals.[21]

We then analyzed the charge-transport properties by four-point conductivity (Figure 2A) and Hall effect measurements using carbon electrodes (Figures S6 – S9, Table S4-S5). While the conductivity of **1Br** was too low to be measured at room temperature (<10^{-8} S cm^{-1}), **1I** exhibited a conductivity of 6(2)×10^{-3} S cm^{-1} and a hole concentration of 1.2(2)×10^{17} cm^{-3}. Further, variable-temperature conductivity for **1I** revealed typical semiconducting behavior (Figure 2), with an activation energy for conduction (E_a) of 0.18 eV. The **1I** charge-transport properties are consistent with those of $(CH_3NH_3)SnI_3$,[7-8, 22] and 2D Sn–I perovskites.[10] Further, **1Br** shows similar transport properties to most Sn–Br perovskites, displaying much lower conductivities than the iodide analogs.[23]

For Sn–I perovskites, Sn^{4+} ions are considered as acceptors (A), characterized by their energy level above the VBM, activation

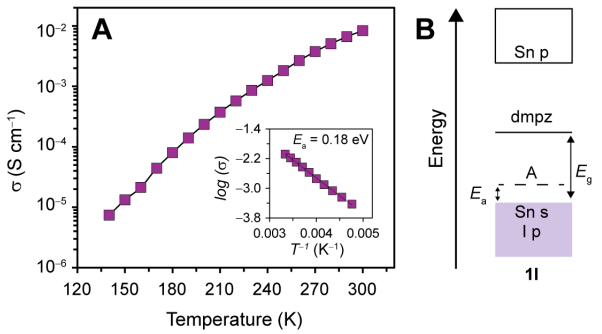

Figure 2. Ambient-pressure charge-transport properties for **1I**. A) Variable-temperature electronic conductivity (σ) for **1I**, and linear fit of the Arrhenius plot (inset), which gives the activation energy for conduction (E_a); B) Schematic band structure for **1I**, displaying the orbital contributions to band extrema, the energy levels of the Sn^{4+}-based acceptor (A) and $dmpz^{2+}$ LUMO, E_a, and the optical gap for transition Ⅰ (E_g).

10.1002/anie.202202911

energy for electron promotion (E_a), and concentration (Figure 2B).[6, 8, 10] Thermal excitation promotes electrons from the VBM to the acceptor (A^0), resulting in ionized acceptors (A^-) and mobile holes in the valence band (in this case, $Sn^{4+} \rightarrow Sn^{2+} + 2h^+$). We estimated the Sn^{4+} acceptor concentration (N_{Sn4+}) using a basic model for doped semiconductors in the ionization regime (Supporting Information).[24] The calculated Sn^{4+} acceptor concentration for **1I** (1.6×10^{18} cm^{-3}) exceeds the valence band hole concentration ($1.2(2)\times10^{17}$ cm^{-3} from Hall-effect measurements), indicating that most acceptors are not ionized at room temperature. Considering the $dmpz^{2+}$ density from the SCXRD structure (2×10^{21} cm^{-3}) and its energy gap to the VBM (0.84 eV), ionization of $dmpz^{2+}$ provides a negligible hole concentration at ambient pressure (8×10^{12} cm^{-3}).

Halide perovskites are highly compressible, with a large electronic response to pressure.[25] Increases in conductivity upon compression occur in a range of halide perovskites including single ($(CH_3NH_3)PbI_3$)[11], double ($Cs_2Au^IAu^{III}X_3$; X = Cl^-, Br^-, I^-)[26-27], and 2D perovskites (R_2CuX_4; R = organic cation, X = Cl^-, Br^-).[28-29] We, therefore, studied the pressure response of **1I**, hypothesizing that the redox activity of dmpz would contribute to its high-pressure properties.

We tracked the pressure-induced structural changes of **1I** by measuring PXRD patterns in diamond-anvil cells (DACs) using Ne as a pressure-transmitting medium. Upon compression, the diffraction peaks of the *α* phase (*Pbam*) of **1I** continuously shifted to higher angles until a phase transition occurred at 5.1 GPa (Figure 3A). Upon further compression, the *β* phase reflections moved to higher angles until the splitting of the peak at ~3.9° indicated a second phase transition around 29 GPa (*β*→*γ*) (Figure S12). We indexed the high-pressure *β* phase to the $P2_1/c$ space group, similar to other Pb- and Sn-based expanded lattices (Table S3), based on observed reflections and systematic absences. However, other space-group/unit-cell assignments are possible. With increasing pressures, the peaks in the **1I** PXRD pattern broaden and then disappear, preventing indexing of the **1I** high-pressure γ phase. A similar amorphization has been reported for most halide perovskites upon compression.[29-32] In a separate experiment without a pressure medium, we compressed **1I** to 35 GPa and then decompressed it to ambient pressure. Upon compression, the PXRD pattern of **1I** showed peak broadening and disappearance as observed in the Ne-loaded PXRD patterns (Figure S17). The PXRD pattern did not fully recover its original sharpness upon decompression, indicating a partial amorphization during the compression-decompression cycle (Figure S17).

We performed Rietveld refinements on the high-pressure PXRD patterns of the *α* phase of **1I**, using atomic coordinates from the ambient-pressure SCXRD structure, and Pawley refinement for the high-pressure *β* phase. We then fitted the unit-cell volume-pressure points to a second-order Birch−Murnaghan equation-of-state (Figure 3B). The bulk modulus of the *α* phase of **1I** (K_0 = 16(1) GPa) revealed that it is highly compressible, like other 3D halide perovskites (K_0 = 12 − 18 GPa).[25]

We then studied the evolution of the optical properties of **1I** up to ~40 GPa by measuring absorption spectra across the visible and near- and mid-infrared (IR) wavelengths under air-free conditions. At 0.6 GPa, the spectrum exhibited an optical absorption onset at ~0.8 eV (Figure S19), matching the ambient-pressure transition I. Transition II could not be observed in the high-pressure spectra because transition I saturated the detector in the visible region. Further, the lower-frequency region of the spectra (0.05 – 0.5 eV) contained IR signals related to vibrations of the $dmpz^{2+}$ bonds, matching its ambient-pressure IR spectrum (Figure S20).

Upon compression, the E_g for the **1I** *α* phase gradually redshifted up to 5.4 GPa and then plateaued around the pressure of the *α*→*β* phase transition (Figure 4A). Above 10 GPa, the E_g gradually redshifted and reached a small value (0.08 eV) at 22 GPa. Metal-halide bond compression, which increases band dispersion, likely explains the E_g redshift for **1I**.[25] In contrast, the tilting of the metal-halide dimers and the resulting loss of band dispersion may explain the plateau in the *α*→*β* phase-transition pressures.

Motivated by the decrease in E_g upon compression, we measured variable-pressure four-point conductivity (*σ*) for **1I** under air-free conditions (Figure 4B). Upon compression, the conductivity rises with pressure up to 50(17) S cm^{-1} at 60 GPa; a pressure-induced increase of five orders of magnitude. The **1I** high-pressure conductivities exceed the values for $(CH_3NH_3)PbI_3$ (6.6 S cm^{-1} at 62 GPa),[11] and $(CH_3NH_3)SnI_3$ (10^{-6} S cm^{-1} at 30 GPa)[31]. We also measured the ambient-pressure conductivity of $(CH_3NH_3)SnI_3$ (20(3) S cm^{-1}) under air-free conditions. We note, however, that a range of ambient-pressure conductivity values has been reported for $(CH_3NH_3)SnI_3$ ($22 \le \sigma \le 143$ S cm^{-1}),[7-8, 33] likely due to changes in hole-doping concentrations.

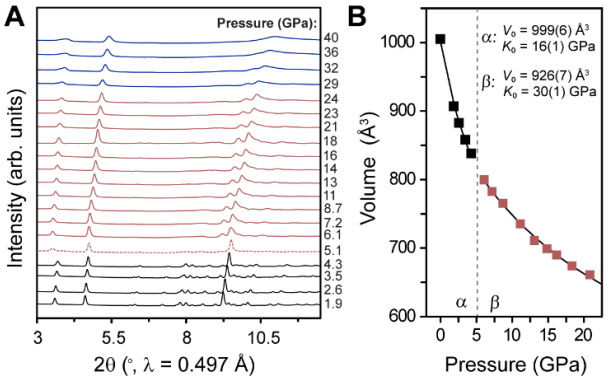

Figure 3. A) Powder X-ray diffraction (PXRD) patterns for **1I** upon compression. Pressure ranges for each phase: *α* (1.9 – 4.3 GPa), *α* + *β* (5.1 GPa), *β* (6.1 – 24 GPa), and *γ* (29 – 40 GPa); B) Unit-cell volume changes upon compression for **1I**. Second-order Birch−Murnaghan equation-of-state fits are shown as black lines, and fit parameters are given for the *α* and *β* phases.

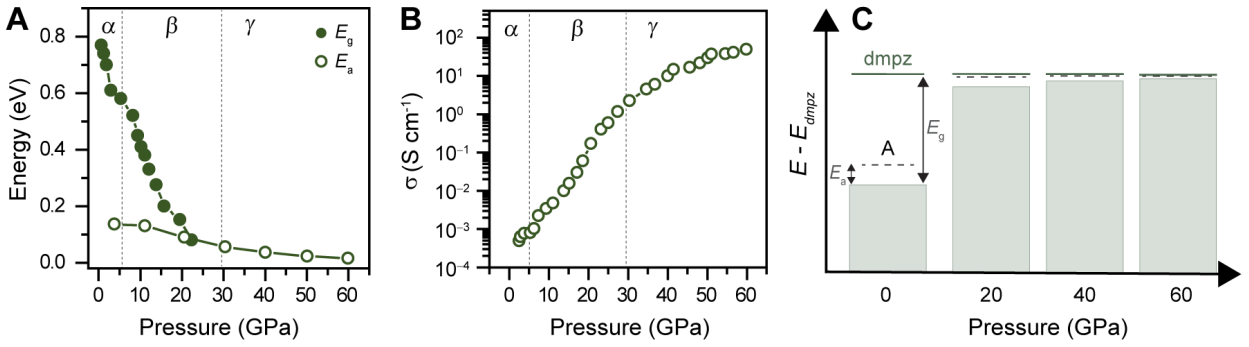

Figure 4. A) Evolution of the optical gap (E_g) and the activation energy for conduction (E_a) with increasing pressure; B) Electronic conductivity (σ) as a function of pressure; C) Schematic representation of the evolution of the relative energies of the VBM, the Sn^{4+}-based acceptor (A), and dmpz LUMO upon compression.

We then measured variable-temperature conductivity at selected pressures (Figure S22). Upon compression, the activation energy (E_a) for **1I**, extracted from the linear fit of the Arrhenius plots, decreases from 0.136 eV (3.8 GPa) to 0.015 eV (60 GPa) (Figure 4A). Upon decompression, **1I** exhibits conductivities one order of magnitude lower than those measured at analogous pressures upon compression (Figure S23).

At ambient pressure, the conductivity of **1I** arises from the ionization (reduction) of the Sn^{4+}-based acceptor level (Figure 4C). Upon compression, the E_a values decrease towards kT (0.026 eV at room temperature), indicating that the Sn^{4+}-acceptors can be fully ionized with increasing pressures (Figure 4A). The simultaneous E_g narrowing (Figure 4A) indicates that thermal energy could promote electrons from the VBM to the $dmpz^{2+}$ LUMO as well, augmenting the hole concentration ($dmpz^{2+} \rightarrow dmpz^{+} + h^{+}$). Indeed, the E_a at 21 GPa (0.09 eV) is similar in energy to the E_g at 22 GPa (0.08 eV). At this pressure, the Sn^{4+}-based two-electron acceptor and the $dmpz^{2+}$ one-electron acceptor lie at very similar energies, and thermally excited valence electrons should be available to both levels. The SCXRD concentration of $dmpz^{2+}$ (N_{dmpz}, 2×10^{21} cm^{-3}) and the Sn^{4+}-based acceptor concentration (N_{Sn4+}, 1.6×10^{18} cm^{-3}) suggest that most holes originate from $dmpz^{2+}$ reduction. Further compression of **1I** to 60 GPa reduces E_a to 0.015 eV, likely increasing the hole concentration owing to the still smaller thermal barrier for ionization.

The pressure-induced reduction of E_g indicates increased valence band dispersion. Thus, we expect that increased hole mobility also contributes to the conductivity enhancement of **1I** upon compression. If $dmpz^{2+}$ ionization did not occur, and if the Sn^{4+} acceptors were fully ionized, the hole mobility should increase up to ~1000 cm^2 V^{-1}s^{-1} (by a factor of ~4×10^3) to reach the observed conductivity. However, the high-pressure PXRD patterns indicate that **1I** losses crystallinity upon compression, especially in the *γ* phase (>29 GPa). Pressure-induced amorphization leads to a drop in conductivity in the closely related $(CH_3NH_3)SnI_3$ perovskite.[31] Furthermore, upon decompression, **1I** does not fully regain crystallinity and displays conductivity values that are one order of magnitude lower than those measured at the same pressures upon compression. Thus, the partial amorphization in the *γ* phase appears to impede mobility. Although we are unable to directly measure the hole concentration at high pressures, as the experimentally measured electron promotion energy to the dmpz states (E_g) becomes competitive with electron promotion to the Sn^{4+} states (E_a) at high pressures, we expect that the high conductivity arises primarily from an increase in hole concentration and not only from an increase in hole mobility.

The pressure-induced conductivity enhancement described here is reminiscent of charge-transfer doping between semiconductors and redox-active molecules. In contrast to previous charge-transfer doping in halide perovskites, **1I** incorporates the redox-active molecules in the crystal structure. Thus, **1**I can be considered to contain a 3D inorganic sublattice and a 0D organic sublattice. The differential pressure response of these two compositionally distinct sublattices causes the VBM to move relative to the dmpz LUMO until dmpz becomes competitive as an electron acceptor. Thus the dmpz cations act as “charge reservoirs”, in analogy to the charge-reservoir layers in superconducting cuprates that transfer carriers to the Cu-O superconducting layers.[34] The molecular nature of the charge reservoirs may allow for the introduction of electron-donating/withdrawing groups to further tune the position of the LUMO without significantly affecting the VBM energy. Such molecular tuning could provide delicate control over the charge-transfer doping mechanism proposed here, potentially reducing the necessary pressure to achieve high carrier concentrations.

Acknowledgments

This work was supported by the Department of Energy (DOE), Office of Basic Energy Sciences (BES), Division of Materials Sciences and Engineering (DE-AC02-76SF00515). High-pressure PXRD data were collected at beamline 12.2.2 at the Advanced Light Source, supported by the Office of Science, BES, DOE (DE-AC02-05CH11231). High-pressure absorption measurements used beamline 22-IR-1 of the National Synchrotron Light Source II, a U.S. DOE Office of Science User Facility operated by the Brookhaven National Laboratory (DE-SC0012704) and supported by COMPRES under the National Science Foundation (EAR 11- 57758) and the Carnegie DOE Alliance Center (DE-FC03-03N00144). N.R.W. was supported by a Stanford Interdisciplinary Graduate Fellowship. We thank Dr. Martin Kunz and Dr. Bora Kalkan for technical assistance, Dr. Rebecca Smaha for helpful discussions, and Prof. Wendy Mao for access to equipment.

Keywords: high pressure • halide perovskite • doping • conductivity • 3D perovskite analogs

References

[1] G. E. Eperon, M. T. Hörantner, H. J. Snaith, *Nat. Rev. Chem.* **2017**, *1*, 95-95.
[2] M. D. Smith, B. A. Connor, H. I. Karunadasa, *Chem. Rev.* **2019**, *119*, 3104-3139.
[3] Q. A. Akkerman, G. Rainò, M. V. Kovalenko, L. Manna, *Nat. Mater.* **2018**, *17*, 394-405.
[4] T. M. Brenner, D. A. Egger, L. Kronik, G. Hodes, D. Cahen, *Nat. Rev. Mater.* **2016**, *1*, 15007.
[5] J. Queisser Hans, E. Haller Eugene, *Science* **1998**, *281*, 945-950.
[6] J. Euvrard, Y. Yan, D. B. Mitzi, *Nat. Rev. Mater.* **2021**, *6*, 531-549.
[7] D. B. Mitzi, C. A. Feild, Z. Schlesinger, R. B. Laibowitz, *J. Solid State Chem.* **1995**, *114*, 159-163.
[8] Y. Takahashi, R. Obara, Z.-Z. Lin, Y. Takahashi, T. Naito, T. Inabe, S. Ishibashi, K. Terakura, *Dalton Trans.* **2011**, *40*, 5563-5568.
[9] S. Gupta, D. Cahen, G. Hodes, *J. Phys. Chem. C* **2018**, *122*, 13926-13936.
[10] Y. Takahashi, R. Obara, K. Nakagawa, M. Nakano, J.-y. Tokita, T. Inabe, *Chem. Mater.* **2007**, *19*, 6312-6316.
[11] A. Jaffe, Y. Lin, W. L. Mao, H. I. Karunadasa, *J. Am. Chem. Soc.* **2017**, *139*, 4330-4333.
[12] D. Umeyama, L. Leppert, B. A. Connor, M. A. Manumpil, J. B. Neaton, H. I. Karunadasa, *Angew. Chem. Int. Ed.* **2020**, *59*, 19087-19094.
[13] H.-Y. Zhang, X.-J. Song, H. Cheng, Y.-L. Zeng, Y. Zhang, P.-F. Li, W.-Q. Liao, R.-G. Xiong, *J. Am. Chem. Soc.* **2020**, *142*, 4604-4608.
[14] Y.-Y. Tang, Y.-H. Liu, H. Peng, B.-B. Deng, T.-T. Cheng, Y.-T. Hu, *J. Am. Chem. Soc.* **2020**, *142*, 19698-19704.
[15] X. Li, Y. He, M. Kepenekian, P. Guo, W. Ke, J. Even, C. Katan, C. C. Stoumpos, R. D. Schaller, M. G. Kanatzidis, *J. Am. Chem. Soc.* **2020**, *142*, 6625-6637.
[16] *CCDC 2154060-2154063 contain the supplementary crystallographic data for this paper. The data can be obtained free of charge from The Cambridge Crystallographic Data Centre via https://www.ccdc.cam.ac.uk/structures/*
[17] L.-y. Huang, W. R. L. Lambrecht, *Phys. Rev. B* **2013**, *88*, 165203.
[18] M. G. Goesten, R. Hoffmann, *J. Am. Chem. Soc.* **2018**, *140*, 12996-13010.
[19] J. Tauc, *Mater. Res. Bull.* **1968**, *3*, 37-46.
[20] R. Matheu, J. A. Vigil, E. J. Crace, H. I. Karunadasa, *Trends Chem.* **2022**, *4*, 206-219.
[21] L. J. Norrby, *J. Chem. Educ.* **1991**, *68*, 110.
[22] Y. Takahashi, H. Hasegawa, Y. Takahashi, T. Inabe, *J. Solid State Chem.* **2013**, *205*, 39-43.
[23] G. S. Lorena, H. Hasegawa, Y. Takahashi, J. Harada, T. Inabe, *Chem. Lett.* **2014**, *43*, 1535-1537.
[24] C. Kittel, 8th ed., Wiley, Hoboken, NJ, pp. 208, 213-214.
[25] A. Jaffe, Y. Lin, H. I. Karunadasa, *ACS Energy Lett.* **2017**, *2*, 1549-1555.
[26] N. Kojima, *Bull. Chem. Soc. Jpn.* **2000**, *73*, 1445-1460.
[27] P. Naumov, S. Huangfu, X. Wu, A. Schilling, R. Thomale, C. Felser, S. Medvedev, H. O. Jeschke, F. O. von Rohr, *Phys. Rev. B* **2019**, *100*, 155113.
[28] A. Jaffe, Y. Lin, W. L. Mao, H. I. Karunadasa, *J. Am. Chem. Soc.* **2015**, *137*, 1673-1678.
[29] A. Jaffe, S. A. Mack, Y. Lin, W. L. Mao, J. B. Neaton, H. I. Karunadasa, *Angew. Chem. Int. Ed.* **2020**, *59*, 4017-4022.
[30] Y. Lee, D. B. Mitzi, P. W. Barnes, T. Vogt, *Phys. Rev. B* **2003**, *68*, 020103.
[31] X. Lü, Y. Wang, C. C. Stoumpos, Q. Hu, X. Guo, H. Chen, L. Yang, J. S. Smith, W. Yang, Y. Zhao, H. Xu, M. G. Kanatzidis, Q. Jia, *Adv. Mater.* **2016**, *28*, 8663-8668.
[32] A. Jaffe, Y. Lin, C. M. Beavers, J. Voss, W. L. Mao, H. I. Karunadasa, *ACS Cent. Sci.* **2016**, *2*, 201-209.
[33] M. A. Haque, L. H. Hernandez, B. Davaasuren, D. R. Villalva, J. Troughton, D. Baran, *Adv. Energy Sustainability Res.* **2020**, *1*, 2000033.
[34] R. J. D. Tilley, *Perovskites : structure-property relationships*, John Wiley & Sons, **2016**, pp. 258-267.

10.1002/anie.202202911

WILEY-VCH

COMMUNICATION

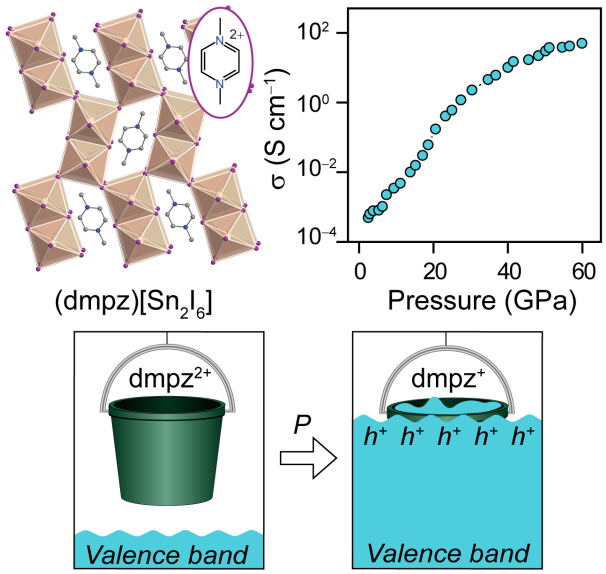

Redox-active organic cations can act as charge reservoirs in the expanded perovskite analog (dmpz)[Sn_2I_6]. Material compression increases electronic conductivity by five orders of magnitude. This conductivity rise is attributed to an increased hole density in the valence band, caused by electron transfer to the redox-active molecules.